Accepted Manuscript

Tumor microenvironment-manipulated radiocatalytic sensitizer based on bismuth heteropolytungstate for radiotherapy enhancement

Ruyi Zhou, Huamei Wang, Yufei Yang, Chenyang Zhang, Xinghua Dong, Jiangfeng Du, Liang Yan, Guangjin Zhang, Zhanjun Gu, Yuliang Zhao

Please cite this article as: Zhou R, Wang H, Yang Y, Zhang C, Dong X, Du J, Yan L, Zhang G, Gu Z, Zhao Y, Tumor microenvironment-manipulated radiocatalytic sensitizer based on bismuth heteropolytungstate for radiotherapy enhancement, *Biomaterials* (2018), doi: https://doi.org/10.1016/j.biomaterials.2018.10.016.

This is a PDF file of an unedited manuscript that has been accepted for publication. As a service to our customers we are providing this early version of the manuscript. The manuscript will undergo copyediting, typesetting, and review of the resulting proof before it is published in its final form. Please note that during the production process errors may be discovered which could affect the content, and all legal disclaimers that apply to the journal pertain.

Tumor microenvironment-manipulated radiocatalytic sensitizer based on bismuth heteropolytungstate for radiotherapy enhancement

Ruyi Zhou, Huamei Wang, Yufei Yang, Chenyang Zhang, Xinghua Dong, Jiangfeng Du, Liang Yan*, Guangjin Zhang*, Zhanjun Gu*, Yuliang Zhao

R. Zhou, H. Wang, Y. Yang, C. Zhang, X. Dong, L. Yan, Prof. Z. Gu, Prof. Y. Zhao
CAS Key Laboratory for Biomedical Effects of Nanomaterials and Nanosafety, Institute of High Energy Physics, Chinese Academy of Sciences, Beijing, 100049, China
E-mail: yanliang@ihep.ac.cn, zjgu@ihep.ac.cn

R. Zhou, H. Wang, Y. Yang, C. Zhang, X. Dong, L. Yan, Prof. Z. Gu, Prof. Y. Zhao
College of Materials Science and Optoelectronic Technology, University of Chinese Academy of Sciences, Beijing, 100049, China

Prof. G. Zhang
Key Laboratory of Green Process and Engineering, Institute of Process Engineering, Chinese Academy of Sciences, 100190, Beijing, China
E-mail: zhanggj@home.ipe.ac.cn

Dr. J. Du
Department of Medical Imaging, First Hospital of Shanxi Medical University, Taiyuan,
Shanxi, 030001, China

Radioresistance resulted from the intrinsic features of tumors often gives rise to unsatisfied therapeutic outcome. In particular, the tumor microenvironment (TME) with abundant antioxidants, elevated hydrogen peroxide (H_2O_2) and hypoxia has been believed as a tremendous obstacle for radiotherapy. Therefore, developing an effective radiosensitizer in response to both X-ray and the TME is highly imperative but remains a challenge so far. Here, we for the first time explore bismuth heteropolytungstate (BiP_5W_{30}) nanoclusters as radiosensitizers for the TME-manipulated enhancement of radiotherapy. On the one hand, BiP_5W_{30} nanoclusters can increase radiation dose deposition within tumors by high-Z elements like Bi and W. On the other hand, in virtue of the unique electron structure and multi-electron property, they have the capability of depleting glutathione (GSH) via redox reaction and catalyzing the decomposition of H_2O_2 to $HO^{\bullet}$ to enhance ROS generation upon X-ray radiation. Moreover, reduced graphene oxide (rGO) coupled with BiP_5W_{30} can further improve radiocatalytic activity through promoting electron-hole separation. Simultaneously, due to the considerable near-infrared absorption of rGO, photothermal therapy can overcome the tumor hypoxia microenvironment and thus synergize with radiotherapy. In addition to providing a promising radiosensitizer, this finding is expected to extend the application of polyoxometalates used in the biomedical field.

1. Introduction

Radiation therapy (RT), as a major modality of cancer therapy, is a local treatment and can effectively suppress tumor non-invasively.[1, 2] To date, tremendous effort has been devoted to improve the radiotherapeutic efficiency via the internal (a radioactive material) or external (high-energy X-rays) strategies.[2-6] However, radioresistance resulted from the intrinsic features of tumors often gives rise to unsatisfied therapeutic outcome and subsequent tumor relapse. In particular, the specific microenvironment of tumor has been believed as the major obstacle of cancer therapy.[7-9] A common concern is the oxygen-deficient microenvironment in solid tumors largely due to the distorted blood vessels and the fast growth of cancer cells,[10] which could develop systemic acquired resistance to radiation and make cancer cells 2-3 times more radioresistant than normoxic tumors.[11,12] Moreover, because the elevation of antioxidants is a general feature of cancer phenotype, antioxidant system (AOS) within cancer cells may prevent them against the damage from radiation via quenching excessive free radicals.[13] For example, the level of glutathione (GSH) within cancer cells is ~4-fold higher than that of the normal cells[14, 15], thus causing the scavenging of reactive oxygen species (ROS) before their arrival at target sites and subsequent great reduction of radiotherapeutic efficiency.[16, 17] Therefore, it is highly desirable to reduce the intracellular GSH level to circumvent tumor resistance and improve RT efficacy.[17] In addition, hydrogen peroxide (H_2O_2) within a tumor is also over-produced due to the insufficient blood supply and rapid metabolism of cancer cells.[18-20] Notably, it has been

approved that ionizing radiation can increase the generation of superoxide ion ($O_2^{\bullet-}$)

by promoting mitochondrial electron transport chain (ETC) and then these free radical

are quickly converted to H_2O_2 with the aid of superoxide dismutase (SOD).[21, 22]

This further elevates H_2O_2 level in cancer cells during the radiotherapy treatment.[23]

Since the above mentioned characteristics of the tumor microenvironment (TME) are

rather unique compared to normal tissues, it is conceivable that, if the TME can be

manipulated by the internal and external stimuli, which points at the improvement of

hypoxia, disturbance of AOS, and conversion of overproduced H_2O_2 into highly toxic

hydroxyl radical (HO$^{\bullet}$), the tumor-specific radiotherapy will be achieved.

Here, for the first time, we show that bismuth heteropolytungstate $[BiP_5W_{30}O_{110}]^{12-}$

(BiP_5W_{30}) nanoclusters, which possess ultrasmall size, well water solubility and

versatile properties can serve as a simple yet powerful radiosensitizer in response to

both external X-ray and the internal TME. **Figure 1** demonstrates the main

therapeutic principles. First, due to the presence of multiple high Z elements such as

Bi and W, BiP_5W_{30} nanoclusters could physically increase X-ray radiation dose

deposition within cancer cells.[24, 25] Moreover, by virtue of the highest oxidation

state of W^{6+}, these nanoclusters have the ability to deplete intracellular GSH pool via

redox reaction between W^{6+} and GSH, leading to overwhelm AOS and increase ROS

level.[26, 27] Most importantly, as one of the promising photocatalysts, BiP_5W_{30}

nanoclusters also have high radiocatalytic activity to produce electron-hole pairs

under X-ray irradiation. Subsequently, the radio-generated electrons could be

transferred to abundant H_2O_2 in the TME, finally yielding HO$^{\bullet}$, one of the most

harmful free radicals.[28] Furthermore, to improve radiocatalytic activity for ROS generation, we couple BiP_5W_{30} nanoclusters with reduced graphene oxide (rGO) to form a heterostructure which is beneficial to promote the electron-hole separation, consequently enhancing the generation of ROS.[29] Besides, the mild photothermal effect caused by rGO under near-infrared (NIR) irradiation is capable of enhancing the intratumoral blood flow, subsequently increasing the concentration of oxygen around the TME. This further decrease the hypoxia-associated radiotherapy resistance and result in the enhancement of radiotherapeutic efficacy.[30] Therefore, the BiP_5W_{30} nanocluster-based radiocatalytic sensitizer with dual response to both X-ray and the TME could not only enhance local X-ray dose deposition within cancer cells but also manipulate the TME for reversing tumor radio-resistance through the depletion of GSH level, radiocatalytic conversion of H_2O_2 into $HO^{\bullet}$, as well as improvement of oxygen level within tumors.

2. Experimental section

2.1 Materials

All of the reagents were analytical grade and used without any further purification. Sodium tungstate dihydrate ($Na_2WO_4 \cdot 2H_2O$, 99.00%), bismuth nitrate pentahydrate ($Bi(NO_3)_3 \cdot 5H_2O$, 99.99%), potassium acetate ($K(CH_3COO)$, 99.00%) and methanol (CH_3OH) were supplied by Alfa Aesar Reagent Co. Poly(vinyl pyrrolidone) (PVP, $M_w \approx 10\,000$) was provided by Sigma Aldrich. Phosphoric acid (H_3PO_4) was purchased from Sinopharm Chemical Reagent Co., Ltd. Potassium chloride (KCl, 99.50%) was

obtained from Aladdin Co. Other reagents were all purchased from Beijing Chemical

Reagent Co.

2.2 Preparation of BiP$_5$W$_{30}$ nanoclusters

K$_{12.5}$Na$_{1.5}$[NaP$_5$W$_{30}$O$_{110}$]•15H$_2$O was prepared according to the reported method

with an improved yield.[31] Typically, Na$_2$WO$_4$•2H$_2$O (16.5000 g) was dissolved in

15.00 mL of deionized water, followed by the addition of 13.25 mL of 85% H$_3$PO$_4$.

The resulting mixture was then heated at 120 °C for 12 h under continuous stirring.

After slowly cooled down to room temperature, 7.50 mL of deionized water and

5.0000 g of solid KCl were sequentially added to the clear yellow solution, obtaining

slightly yellow milk-like mixture. The crude product was filtered, washed with 2 M

potassium acetate and methanol, and dried at 60 °C in the vacuum oven for 24 h. To

further remove the remaining metal species, the obtained product was dissolved in an

appropriate hot-water, making a saturated solution. The solution was then cooled

down to room temperature to obtain white pin-shaped crystals. A second

recrystallization gave the pure product with the same protocol as described above.

Bismuth heteropolytungstate nanoclusters were synthesized through the ion

exchange reaction conducted under hydrothermal conditions. In detail, 2.0000 g of

K$_{12.5}$Na$_{1.5}$[NaP$_5$W$_{30}$O$_{110}$]•15H$_2$O was dissolved in a 24-mL deionized water

containing 0.16-mL HCl, and the solution was heated to 60 °C under vigorous stirring

to obtain a homogeneous suspension. Then, 6-mL dispersion of Bi(NO$_3$)$_3$•5H$_2$O

(0.2328 g) was dropwise added into the above solution under vigorous stirring. The

obtained mixture was transferred into a 45-mL stainless Teflon-lined autoclave and heated at 160 °C for 12 h. When the autoclave was allowed to cool to room temperature naturally, 8.0000 g of solid KCl was added into the mixture to predicate the product. Finally, the colorless product was collected by filtration, washed several times with ice water, and dried at 60 °C for 24 h.

2.3 Preparation of graphene oxide nanosheets

Graphite oxide was synthesized by a modified Hummer's method.[32, 33] In detail, graphite flakes were oxidized with $KMnO_4$ in the presence of concentrated H_2SO_4. After vigorous stirring at 37 °C for 2 h, the appropriate deionized water and 30% H_2O_2 were sequentially added into the mixture. Graphite oxide was achieved by centrifugation and washed several times with deionized water (containing 5% hydrochloric acid). The obtained precipitate was then dispersed in deionized water again and then subjected to dialysis for two weeks to remove any residual metal ion and acid. In order to exfoliate graphite oxide, the product was diluted with deionized water until the final concentration reached to ~1 mg/mL, followed by sonication for 20 h with a probe sonicator. Finally, the obtained dispersion was centrifuged at 12 000 rpm for 10 min, and the supernatant containing graphene oxide (GO) was obtained.

2.4 Preparation of PVP-functionalized hybrid composed of BiP_5W_{30} nanoclusters and reduced graphene oxide

The hybrid composed of BiP_5W_{30} nanoclusters and reduced graphene oxide (rGO) was prepared via the electrochemical reduction process (ERP).[34] In a typical

synthesis, BiP_5W_{30} nanocluster (0.2000 g) was dissolved into 0.5 M H_2SO_4 solution (15.32 mL, as the electrolyte solution), followed by the addition of the aqueous dispersion of GO (4.68 mL, ~2.0 mg/mL) under stirring, forming a homogeneous suspension. Then, controlled potential coulometry measurement was performed in a three-electrode conventional glass cell with the mixture of BiP_5W_{30} nanoclusters and GO. In this system, a glassy carbon (GC) plate was applied as the working electrode, a platinum sheet with large surface area as the counter electrode, and a saturated calomel electrode (SCE) as the reference electrode. More importantly, SCE and platinum sheet must be separated from the electrolyte by a glass frit. After saturation of the electrolyte with ultrahigh-purity argon (Ar) gas for 0.5 h, a potential of -0.62 V vs. SCE was set on the working electrode to fully reduce BiP_5W_{30} nanocluster by 10 electrons. When the electrochemical reduction was completed, the mixture changed to dark-blue and then stood for several hours until the dark-blue color was disappeared. Then, the suspension was washed several times with ultrapure water and then dialyzed with a dialysis bag (MWCO: 3.5 kDa) for 48 h to remove free ions. (named as PG) To improve the biocompatibility and dispersibility of the synthesized PG, 0.0025 mg of PVP was added into 10 mL of PG (in term of GO, 1 mg/mL). After vigorous stirring for 24 h, the product was collected by configuration, washed several times with deionized water, and finally stored at 4 °C. (named as PVP-PG)

2.5 Photocurrent Measurement

The interdigitated electrodes (IDE) of gold/chrome (Au/Cr) device were used to measure the X-ray-induced photocurrent. Typically, the as-prepared BiP_5W_{30} or

PVP-PG deposited on the IDE with 20-µm electrode gap. (0.2 mg/mm^2) Then, photoresponse on Au/Cr IDE was performed by using an X-ray tube with the voltage of 50 kV and the current of 75 µA for all experiments. (Mini-X, AMPTEK Inc.) Both X-ray-induced and dark currents from the BiP_5W_{30} or PVP-PG were measured by using the following conditions: 80 s period of on/off X-ray by six times, 10-V bias voltage.

2.6 Electrochemical measurement

Electrochemical measurement was conducted in the acidic electrolyte (0.5 M H_2SO_4) and controlled using a CHI 660D electrochemical workstation (CHI Instrument, Inc.). A standard three-electrode setup was used in all experiments: reference electrode (SCE), working electrode (an indium-tin oxide, ITO), and a counter electrode (a platinum sheet). When 0.1000 g of BiP_5W_{30} was dispersed into 10-mL 0.5 M H_2SO_4, the electrolyte was thoroughly degassed with Ar gas for 0.5 h and then flushed with Ar gas to prevent oxygen from dissolving into the electrolyte. The electrochemical measurement was carried out with a scan rate of 10 mV/s.

2.7 Detection of hydroxyl radical

The radio-catalytic generation of hydroxyl radical (HO$^\bullet$) by PVP-PG under X-ray irradiation was examined by the HO$^\bullet$-specific indicator[35] (terephthalic acid, TA, 5 mM, Alfa Aesar), which can react with HO$^\bullet$ to form 2-hydroxy terephthalic acid (TAOH, the maximum fluorescence peak at 435 nm). The solution of TA was first added into the control, PVP-PG, X-ray, and PVP-PG+X-ray, respectively, in the absence or presence of H_2O_2 (1 mM). After irradiation with/without X-ray (50 kV, 75

μA, 10 min), the mixtures were gently shaken at 37 °C for 12 h in the dark, and then changes of fluorescence emission at 435 nm were recorded. The method of active species trapping experiment is similar to the radio-activity test, but the electron scavenger ($Na_2S_2O_8$, 0.2 mM) is added.

2.8 Detection of hydrogen peroxide *in vitro*

For the detection of relative content of H_2O_2 within HeLa cells, cells were seeded in 6-well plate at a density of 5×10^5 cells/well with complete medium for 24 h, and then treated with or without PVP-PG (12 μg/mL). After incubation for 6 h, different groups were irradiated with or without X-ray and then incubated for another 6 h. The cells were collected by centrifugation and washed twice with PBS. With the addition of 100 μL of Lysis Buffer of H_2O_2, the cells were homogenized and centrifuged at 12000 g for 4 min at 4 °C. Finally, 50-μL supernatants and 100-μL test solutions (hydrogen peroxide assay kit, Beyotime) were mixed in 96-well plate, placed at room temperature for 0.5 h, and measured immediately with a microplate spectrophotometer at the wavelength of 570 nm.

For the confocal fluorescence imaging, HeLa cells were seeded in glass bottom confocal dishes at a density of 2×10^5 cells/dish with complete medium for 24 h, and then incubated in the presence or absence of PVP-PG (12 μg/mL). After 6 h, different groups were treated with or without X-ray and incubated for another 3 h. Then, cells in different groups incubated with mixture solution for 30 min according to the protocol of assay kit (Fluorimetric Hydrogen Peroxide Assay Kit Infra-red (IR)

Fluorescence, Sigma-Aldrich). When treated with Hoechst for 15 min, the cells were monitored by confocal microscope.

2.9 Detection of hydroxyl radical *in vitro*

To determine the formation of hydroxyl radical, specific hydroxyl radicals ELISA assay (Sensitivity: 0.10 ng/mL) was used to detect the intracellular generation of HO$^{\bullet}$.[36] The kit applies double-antibody one-step sandwich enzyme-linked immunosorbent assay (ELISA). The test antibody and the standard are incubated together with HRP-labeled detection antibody in human hydroxyl radical (HO$^{\bullet}$) capture antibody pre-coated microplates. The microplates are incubated and then washed thoroughly. Then, the microplates are incubated with a substrate TMB for HRP enzyme, which forms a blue colored complex by the enzyme-substrate reaction. Finally, a stop solution is added to stop the above reaction, turning the solution yellow. A microplate reader is used to spectrophotometrically measure the intensity of color (450 nm). Because HO$^{\bullet}$ from HO$^{\bullet}$-HRP conjugate and samples compete for the anti-HO$^{\bullet}$ antibody binding site, the intensity of the color is inversely proportional to the HO$^{\bullet}$ concentration. HeLa cells were plated in 6 well plates at 3×10^5 cells/well overnight and then the cells were pretreated with PVP-PG (12 μg/mL) for 6 h. After that, the cells were irradiated with X-ray for 15 min and then incubated for another 2 h. Then the cells were washed three times with PBS and collected in 1.5 mL centrifuge tube. In an attempt to dissociate the cells and release endogenous components, the cells were lysed with a RIPA lysis (Beytime) and centrifugated at 1000 g for 20 min at 2-8 ℃. Finally, the supernant of different groups were collected

2.10   Ellman's Assay

Glutathione (GSH) oxidation was examined by Ellman's assay and all experiments were conducted in the dark. Ellman reagent (5, 5'- dithiobis (2-nitrobenzoic acid), DTNB, 100 mM, Alfa Aesar) is able to cleave the disulfide bonds (-S-S-) to obtain a yellow product (2-nitro-5 thiobenzoate acid). Typically, the dispersion of PVP-PG (BBS, 100 μg/mL, 225 μL) was mixed with the GSH solution (1.0 mM, 225 μL). The control group is GSH solution. After irradiation with/without X-ray for 10 min, the mixtures were incubated at 37 °C for 0.5, 1, 1.5, 2, 4, and 6 h, respectively. Afterward, 785 μL of 0.05 M Tris-HCl (pH=8.8) solution and 15 μL bicarbonate buffer solution (50 mM, pH=8.77) with DTNB (100 mM) were added into the above mixtures to react for 5 min. After centrifugation at 12 000 rpm for 10 min, the absorbance of supernatants at 410 nm was recorded on a microplate spectrophotometer (Multiskan MK3, Thermo fisher Scientific, England).

2.11   Detection of reactive oxygen species

The catalytic activity of PVP-PG under X-ray irradiation was assessed using a reactive oxygen species (ROS) probe 2',7'-dichlorodihydrofluorescein diacetate (H$_2$DCF-DA, 10 μM, Beyotime Co, Sigma-Aldrich, USA)[37] which can be deacetylated to form H$_2$DCFH and oxidized to form a highly fluorescent 2',7'-dichlorofluorescein (DCF) by ROS. Firstly, 0.5-mL stock solution of H$_2$DCF-DA in dimethyl sulfoxide (DMSO) was mixed with 2-mL 0.01 M NaOH in

the dark. After stirring for 0.5 h at room temperature, the reaction was stopped by adding 10-mL phosphate buffer saline (PBS, 25 mM, pH7.20). Finally, the resulting solution contained 10 μM H_2DCFH, and was wrapped by aluminum foil and kept on ice before use. Then, PBS, PVP-PG, X-ray, and PVP-PG+X-ray were mixed with H_2DCFH solution, respectively. After irradiation with X-ray for 15 min, the dispersion of individual group was centrifuged at 12 000 rpm and the fluorescence of the supernatant was measured by a fluorescence spectrophotometer (Horiba FluoroLog-3, Japan).

2.12 Detection of ROS generation *in vitro*

HeLa cells were incubated in glass bottom confocal dishes at a density of 2×10^5 cells/dish with complete medium for 24 h, and then treated with or without complete medium containing BiP_5W_{30} nanoclusters (80% loading on rGO, 10 μg/mL) and PVP-PG (12 μg/mL). The treated cells were washed twice with PBS and then incubated with H_2DCFH-DA containing RPMI medium for 20 min. When washed with fresh medium, groups were treated with or without near-infrared (NIR) light (808 nm laser, 1 W/cm^2) for 10 min and/or X-ray (50 kV, 75 μA) for 15 min. Finally, the cells were treated with Hoechst 33342 (Beyotime) for 15 min and the fluorescence images of the cells were monitored by the confocal microscope (A1/LSM-Kit, Nikon/PicoQuant GmbH, Japan/Germany).

2.13 Study of effect of GSH level on radiotheraputic outcome

HeLa cells were incubated in a 96-well plate at a density of 5×10^3 cells per well for 24 h. To regulate the level of GSH, the cells were first treated with 500 μM lipoic acid

(LPA, a GSH synthesis enhancer) for 24 h and 2 μM N-methylmaleimide (NMM, a GSH scavenger) for 20 min, respectively. Then, cells were incubated with PVP-PG (12 μg/mL) for 6 h, and subsequently irradiated with X-ray (50 kV, 75 μA) for 15 min. After 24-h incubation, cell viability of HeLa cells was assayed by CCK-8 assay by microplate spectrophotometer.

2.14   Determination of GSH/GSSG ratio *in vitro*

The total glutathione and oxidative glutathione were determined by GSH/GSSG assay kit (Beyotime).[37] For intracellular determination, HeLa cells were incubated in 6-well plate at a density of 1×10^5 cells/well for 24 h and then incubated with PVP-PG (12 μg/ml) for 12 h. The treated cells were irradiated with X-ray for 15 min and then incubated for another 6 h. The cells were collected by centrifugation at 12 000 rpm for 5 min at 4 °C and added with 3× protein solution M. After vortex sufficiently, the mixed solutions were frozen and thawed twice using liquid nitrogen and 37 °C water, respectively. The samples were placed at 4 °C for 5 min and then centrifuged at 10 000 rpm for 10 min at 4 °C. Finally, the supernatant was used for GSH and GSSG assay, and GSH/GSSG was determined according to the manufacturer's instructions.

2.15   *In vitro* colony formation assay

Colony formation assay is an assay of the survival ability of a single cell to grow into a colony *in vitro*. HeLa cells with different numbers (125, 250, 500, 1000, and 2000 cells) were incubated in a 6-well plate with complete medium for 24 h. After attachment, the cells were treated with complete medium containing PVP-PG (12

μg/mL). After incubation for 6 h, the cells were treated with 808-nm laser (1 W/cm^2) and/or X-ray (0, 2, 4, 6, and 8 Gy) and incubated with complete medium for 10 d. Finally, colonies were stained with Giemsa dye (Beijing Solarbio Science & Technology Co., Ltd) and evaluated the effects of different treatments with the survival fraction.

2.16   *In vitro* DNA double-strand breaks assay

HeLa cells were seeded on cover glass and then incubated in 24-well plate at a density of 3×10^4 cells/well. After attachment for 24 h, the cells were treated with or without complete medium containing PVP-PG (12 μg/mL) and then treated with 808-nm laser (1 W/cm^2) and X-ray (50 kV, 75 μA, 10 min). The treated cells were fixed with 4% paraformaldehyde (500 μL/cell) for 10 min after 30 min. When washed three times with PBS, the cells were blocked in 5% FBS and 1% tritonX-100 in PBS (300 μL) for 1 h, and then stained with anti-γ-H2AX antibody (Proteintech Group Inc. Co., Ltd., China) containing 5% FBS and 1% tritonX-100 overnight at 4 °C. Finally, the cells were incubated with the secondary antibody anti-rabbit AlexaFluor-488 conjugated IgG (Abcam) for 1 h and then stained with Hoechst for 15 min. Images were visualized with the confocal microscope. A semiquantitative analysis was used to evaluate the number of foci per cell expressing the γ-H2AX markers.

2.17   *In vitro* apoptosis analysis by flow cytometry

The apoptosis of the cells was detected using the Annexin V-FITC apoptosis detection Kit (Beyotime). Briefly, HeLa cells were seed in 24-well plates with a density of 5×10^4 cells/well for 24 h. After treated with or without PVP-PG (12

μg/mL), different groups were irradiation with or without an 808-nm NIR laser (808 nm laser, 1 W/cm^2) and X-ray (50 kV, 75 μA, 10 min). Then, cells were collected by trypsinization (without EDTA), washed twice with PBS, re-suspended in Annexin V binding buffer and further incubated in Annexin V and PI at room temperature for 15 min in the dark. Finally, cells were subjected to flow cytometry analysis (BD Accuri C6, USA).

2.18   Photothermal therapy/radiotherapy synergistic treatment *in vivo*

For *in vivo* therapy, seven randomly divided groups of HeLa tumor-bearing mice were employed for photothermal therapy/radiotherapy synergistic performance: (I) Control, PBS; (II) NIR; (III) PVP-PG; (IV) PVP-PG+NIR; (V) X-ray; (VI) PVP-PG+X-ray and (VII) PVP-PG+NIR+X-ray. Once the tumors attained 80-100 mm^3, mice were administrated with 20-μL solution of PBS (groups I, II and V) or PVP-PG (2 mg/mL, other groups) via intratumor injection, respectively. Group (II) and (IV) was treated with 808-nm NIR laser (0.35 W/cm^2, 10 min), groups (V) and (VI) were treated with X-ray (6 Gy), and group (VII) was first treated with 808-nm NIR laser (0.35 W/cm^2, 10 min) and then X-ray (6 Gy). The temperature profiles were recorded in real time using a thermal camera during laser irradiation treatment. Following each treatment, the data of body weight and tumor volumes in each group were recorded over the course of 25 d.

2.19   Blood and histology examinations

Each group with five mice at different treatments were euthanatized on 3rd and 25th day after administration. Standard procedures for blood routine examination were

performed with blood obtained from mice on 25th day. In addition, the tumor, heart, liver, spleen, lung, and kidneys were collected for hematoxylin and eosin staining (H&E). Images were collected using an inverted fluorescence microscope.

2.20 *In vivo* **DNA damage study**

DNA damage was evaluated semi-quantitatively by γ-H2AX. First, tumors were harvested and fixed in 10% formalin followed by paraffin embedding. Then, the staining was carried out on tissue sections. To quantify the toxicity by γ-H2AX, the primary antibody and secondary antibody were utilized. Images were analyzed using an inverted fluorescence microscope.

3 Results and discussion

3.1 Synthesis and characterization of PVP-PG

Figure 2a shows how we combine the significant features of rGO and BiP_5W_{30} nanoclusters to form a simple yet efficient radiosensitizer. First, stable BiP_5W_{30} nanoclusters were successfully synthesized according to the previous method,[31] as demonstrated by the results of Fourier transform infrared (FT-IR) and X-ray photoelectron spectroscopy (XPS). **(Figure S1-2)** In these nanoclusters, five PW_6O_{22} units derived from the Keggin anion $[PW_{12}O_{40}]^{3-}$ arrange in a crown and bismuth ion is positioned in it.[31] **(Figure S3)**. From ultraviolet-visible analysis, the structure of BiP_5W_{30} nanoclusters was rather stable in various solutions. **(Figure S4-5)** Then, these nanoclusters were anchored on the surface of graphene nanosheets through an electrochemical method,[34] obtaining BiP_5W_{30}/rGO hybrid (PG). **(Figure S6a-h)** In

particular, the content of BiP_5W_{30} nanoclusters coupled with rGO could fine-controlled by changing the initial ratio of rGO and BiP_5W_{30} nanoclusters in the dispersion. (**Figure S6i**) During this process, graphene oxide (GO) was reduced to form high conductive rGO that is capable of enhancing radiocatalytic activity.[38] (**Figure S7-8**) Remarkably, the thickness of rGO nanosheets (~0.5 nm) increases to ~1.5 nm, which indicates the successful loading of BiP_5W_{30} nanoclusters on the rGO surface. (**Figure 2b, Figure S9**) Finally, to improve the colloidal stability and biocompatibility, PG was further functionalized with PVP,[39] named as PVP-PG. (**Figure 2g, Figure S10**) Transmission electron microscope (TEM) image shows that BiP_5W_{30} nanoclusters are still evenly distributed onto the surface of `graphene nanosheets, in accordance with Raman spectrum analysis. (**Figure 2c, Figure S11**) Energy dispersive X-ray spectroscopy (EDS) analysis demonstrates the homogeneous distribution of Bi, P and W elements on the surface of rGO, which is also verified by XPS analysis. (**Figure 2d-f, Figure S12**) Moreover, PVP-PG possesses a high zeta potential value (-35 mV) and exhibits exceptional stability in biofluids and good biocompatibility. (**Figure 2h, Figure S13**)

3.2 Radiocatalysis effect of PVP-PG

Polyoxometalates (POMs), the well-defined metal-oxygen clusters, have been approved to possess desirable reversibility in multi-electron redox reaction, which enables them with attractive photocatalytic properties.[40, 41] Similar to semiconductor nanoparticles, the electron structure of POMs consists of the highest occupied molecular orbital mainly localized on oxygen atoms (HOMO, like valence

band in semiconductor) and the lowest unoccupied molecular orbital mainly localized on d^0 or d^1 transition metal atoms (LUMO, like conducive band in semiconductor).[42, 43] When POMs are irradiated by an appreciate light (usually in ultraviolet region) with energy equal to or higher than their gap (HOMO-LUMO gap), electrons could be excited from HOMO to LUMO, generating highly reactive electron-hole pairs.[41] Subsequently, these excited electrons and holes are trapped in surface sites and react with surrounding water and/or other molecules via either reductive (electron) or oxidative (hole) pathways.[44] Consequently, the generated free radicals can cause indirect damages to cellular components like DNA, proteins and lipids.[45] It is worth noting that if the energy level of POMs matches with the potential of H_2O_2, they could catalyze low-toxic H_2O_2 to generate $HO^{\bullet}$.[28] This offers an opportunity to use overproduced H_2O_2 within the TME to improve the therapeutic effects. However, due to the strong light scattering and absorption by skin and tissue, the low-energy photons (from ultraviolet to visible regions) cannot penetrate into human body. This greatly limits their application to eradicate deep located tumors.[46, 47]

Recently, several attempts have been devoted to fabricate high Z semiconductors capable of generating ROS under X-ray irradiation.[48, 49] Inspired by this trend, we for the first time explore the possibility of using PVP-PG as an X-ray trigged photocatalyst for RT enhancement because of its well radiocatalytic property and high X-ray absorption ability. The optical band gap of PVP-PG was evaluated by ultraviolet-visible diffuse reflectance spectroscopy (DRS). **(Figure 3a)** PVP-PG exhibits strong absorption in the ultraviolet region. Based on the Tauc plot of

transformed Kubelka-Munk function versus the photon energy, the optical band gap (E_g) of PVP-PG was thus determined to be 2.76 V.[50, 51] Then, the photocurrents generated from both BiP_5W_{30} and PVP-PG shows rapid response during X-ray switching on/off, indicating the electron-hole separation.[49, 52] **(Figure 3b)** Notably, the BiP_5W_{30}/rGO heterojunction structure (PVP-PG) is able to generate significant photocurrent that is about 4-fold higher than that of single BiP_5W_{30} nanoclusters. The higher photocurrent response of PVP-PG to X-ray indicates more efficient separation of radio-generation electron-hole pairs due to rGO with two-dimensional planar structure which can facilitate electron transportation.[29] As a consequence, these radiogenerated electrons and holes are able to initiate the chemical reactions because of the strong photo-oxidative ability of the holes and photo-reductive ability of the electrons.[41] Encouraged by this, we used the energy levels of PVP-PG to predict whether the abundant components like H_2O_2 or H_2O in the TME can react with electrons and/or holes. Based on the fact that redox potential of first reduction peak corresponds to the energy of the LUMO level (mainly the W atoms), the value of LUMO is measured to be 0.10 V vs SHE (standard hydrogen electrode) by cyclic voltammetry.[53] **(Figure 3c)** The energy level of HOMO is thus estimated at 2.86 V from $E_g + E_{LUMO}^{\theta}$. Considering the acidic pH of the TME, all these values were converted to electrochemical potentials at pH 5.00 and 6.50 using Nernst equation.[54] **(Table S1)** According to the results achieved above, we further investigated electron transfer process for radiocatalytic reactions. **(Figure 3d)** Under X-ray irradiation, the absorption of energy by BiP_5W_{30} can excite electrons from HOMO to LUMO to rGO,

leaving positive holes behind. As calculated, the LUMO energy level of PVP-PG is lower than the potential of $O_2/O_2^{\cdot-}$, but higher than that of $H_2O_2/HO^{\cdot}$. Hence, the radio-generated electrons could not be accepted by O_2, but caught by intracellular H_2O_2 for an oxidation reaction to form $HO^{\cdot}$. In parallel, since the HOMO energy level of PVP-PG is lower than the potential of $HO^{\cdot}/H_2O$, the corresponding holes also diffuse to the surface and accept by H_2O for a reduction reaction to produce $HO^{\cdot}$. Therefore, the main contribution of the resulting ROS generated by PVP-PG may be $HO^{\cdot}$.

To examine $HO^{\cdot}$ generation from radiocatalytic reactions, the $HO^{\cdot}$-specific indicator was used in the presence of PVP-PG and/or H_2O_2. There is almost no fluorescence without X-ray irradiation in the presence of PVP-PG. With X-ray irradiation, the fluorescence of 2-hydroxy terephthalic acid[35] (TA-OH, produced by the specific reaction of terephthalic acid with $HO^{\cdot}$) in the presence of PVP-PG increases 1.41-fold higher compared to the control without PVP-PG. **(Figure 3e)** Moreover, the addition of H_2O_2 leads to 1.76-fold fluorescence enhancement under X-ray irradiation. It is clear that both H_2O_2 and H_2O are able to capture radio-generated electrons and holes, respectively, to form high active $HO^{\cdot}$. This is further demonstrated by the trapping experiment which was conducted in the presence of $S_2O_8^{2-}$ scavenger (It can react with electron to yield SO_4^{2-}). [42] **(Figure 3f)** To further verify radio-catalytic activity of PVP-PG, the *in vitro* $HO^{\cdot}$ generation was evaluated. Given that the intracellular H_2O_2 was the source of $HO^{\cdot}$, its content was first determined by hydrogen peroxide assay kit. Remarkably, H_2O_2 level significantly

increases upon X-ray irradiation, which is ascribed to ionizing radiation as mentioned before. **(Figure 3g)** It is noted that H_2O_2 level also increase after incubation with PVP-PG, which may be attributed to the depletion of intracellular GSH pool.[55] However, it clearly decreases under X-ray irradiation in the presence of PVP-PG, indicating the feasible consumption of H_2O_2 by radio-catalytic reaction. This can be further demonstrated by fluorimetric hydrogen peroxide assay kit which can specifically measure hydrogen peroxide. **(Figure 3h)** Furthermore, the content of $HO^{\bullet}$ within cancer cells was directly detected by specific hydroxyl radicals ELISA assay.[36] **(Figure 3i)** Once combining PVP-PG with X-ray irradiation, the concentration of $HO^{\bullet}$ shows about 1.30-fold higher compared to the control. This demonstrates the speculation of radio-catalytic effect and the foregoing results. Therefore, both the theoretical and experimental results confirm that PVP-PG has the ability to convert non-toxic H_2O and low-toxic H_2O_2 into highly active $HO^{\bullet}$ under X-ray irradiation, which contributes to the enhancement of RT.

3.3 Redox effect of PVP-PG

Apart from the radiocatalytic ability to enhance ROS generation, PVP-PG also has the potential for depleting GSH. As we mention before, GSH is critical to protect against ROS and plays an important role in radiation and chemical drug resistance of cancer cells.[56] Depletion of overexpressed GSH within cancer cells could increase the amount of ROS arrived at the target sites to enhance the therapeutic outcome.[37, 57, 58] For BiP_5W_{30}, multi-electron redox activity of transition metal W^{6+} makes a possibility of electrons transfer reactions between GSH and W^{6+}, leading to consume

the intracellular GSH. From the XPS results of elemental states of W atoms, two peaks arising from 4f5/2 and 4f7/2 are observed, evidencing the characteristic +6 oxidation state. (**Figure 2f**) As expected, the potential of GSSG/GSH couple is higher than the energy level of W^{6+} (LUMO), which makes electrons thermodynamically favorable transfer from GSH to W^{6+} and leads to redox reaction to deplete GSH. (**Figure 4a**) The content of GSH under various treatments was quantitatively measured by using Ellman's assay. (**Figure 4b-c**) The control with only GSH in buffer has no change even after 6 h, while GSH is gradually consumed in the presence of PVP-PG, indicating the occurrence of redox reaction, but not some physical changes. To investigate the influence of GSH on ROS generation, detection of ROS under X-ray irradiation with or without GSH was monitored and quantified by 2',7'-dichlorodihydrofluorescein diacetate (H_2DCFDA) which can measure the total amount of ROS, including H_2O_2, $HO^{\bullet}$, and $O_2^{\bullet-}$. (**Figure 4d**) Note that there is almost no fluorescence without X-ray irradiation. Under X-ray irradiation, it is found that the fluorescence of the indicator is remarkably enhanced in the control. This is not surprising because ionizing radiation is known to produce ROS through water radiolysis. More interestingly, though the cells treated with PVP-PG plus X-ray irradiation show lower H_2O_2 level than those treated with PVP-PG only, far more $HO^{\bullet}$ could be produced from H_2O_2 and H_2O under X-ray irradiation, resulting in the highest level of ROS among these groups. However, the fluorescence intensity dramatically decreases in the presence of GSH, indicating that GSH could indeed deplete ROS to a large extent. Importantly, the fluorescence enhancement (F/F_0) of

PVP-PG under X-ray is 1.71-fold higher than that of the control. In the presence of GSH, PVP-PG still could achieve 1.38-fold ROS than that of the control. Moreover, the amount of generated ROS is radiation time-dependent. **(Figure S14)**

To further verify radiocatalytic effect and redox effect of PVP-PG, the *in vitro* ROS generation and GSH depletion was evaluated. Firstly, qualitative image analysis of ROS generation was performed on fluorescence microscopy images of cancer cells pre-treated with H_2DCFDA. As shown in **Figure 4g**, HeLa cells treated with PVP-PG plus X-ray show much higher fluorescence intensity than those only irradiated by X-ray or incubated with PVP-PG. Simultaneously, PVP-PG plus X-ray showed better ability of ROS generation than BiP_5W_{30} nanocluster plus X-ray, resulting in more excellent radiotherapeutic performance as demonstrated by clonogenic assay. **(Figure S15)** This can be attributed to an increased in the yield efficiency of electron-hole pairs because rGO facilitates electron transportation as mentioned before. Next, to test whether GSH depletion can sensitize cancer cells to ROS, we assessed the cell viability under different treatments in the presence of a-lipoic acid (LPA, a GSH synthesis enhancer) or N-methylmaleimide (NMM, a GSH scavenger).[59] As shown in **Figure 4e,** the viability of HeLa cells treated with PVP-PG and NMM is markedly lower than that of cells incubated with PVP-PG alone, while a distinct increase of cell viability is observed when HeLa cells were treated with LPA. These results clearly indicate that the cytotoxicity of PVP-PG can be potentiated by depleting intracellular GSH. Moreover, the ratio of GSH to oxidized glutathione (GSSG) was determined to verity the redox activity of PVP-PG for overwhelming AOS *in vitro*.[37] **(Figure 4f)**

It is found that PVP-PG cause a significant decrease in the cellular GSH/GSSG ratio compared with the group irradiated by X-ray. Therefore, we can infer PVP-PG is capable of diminishing GSH level, causing the increase of ROS level, and subsequently enhancing the outcome of radiotherapy.

3.4 PTT and RT synergetic therapy *in vitro*

Based on the radiocatalytic activity for ROS generation and redox activity for GSH depletion, we evaluated the radiotherapeutic inhibitory activities of PVP-PG on HeLa cells. First, the result of cell colony formation indicates that PVP-PG can significantly enhance the radiation-induced inhibition of a single cell to grow into a colony.[60] (**Figure 5a**) For instance, the survival fraction of HeLa cells treated by X-ray or PVP-PG alone are 71% and 91%, respectively. (**Figure 5d**) After co-treated with X-ray and PVP-PG, the survival fraction dramatically declined to 25%. The clonogenic survival assay was also performed to evaluate *in vitro* radiotherapy enhancement. (**Figure 5e**) Similarly, the group treated with PVP-PG shows much lower percentage of viable cell colonies than that without PVP-PG treatment, even at the same X-ray irradiation dose. The sensitizer enhancement ratio of PVP-PG plus X-ray irradiation was calculated to be 1.41 using a linear-quadratic model. (**Table S2**) The above results suggest the enhancement of radiation effects of PVP-PG, and similar results were also found in A549 cells (**Figure S16**). Since ROS-induced DNA damage was the main contribution for radiation enhancement, immunofluorescently labeling for γ-H2AX was conducted to evaluate DNA double-strand breaks.[61] (**Figure 5b**) Consistent with the cell colony assay result, PVP-PG plus X-ray

produces the higher level of DNA damage compared to radiotherapy alone, indicating that X-ray triggered generation of ROS by PVP-PG could remarkably enhance DNA damage and subsequently inhibit proliferation of cancer cells. **(Figure 5f)** In addition, Fluorescein-annexin V and propidiumiodide staining assays suggest that the cellular toxicity is associated with apoptosis and necrosis. It clearly shows that irradiation of PVP-PG with X-ray leads to more dead cells than the control even in 24 h. **(Figure 5c)** Apart from its ability for radiotherapy enhancement, PVP-PG also has a potential for photothermal therapy (PTT) upon NIR laser irradiation because of the considerable absorbance of rGO in the NIR region.[62] **(Figure S17)** From the evaluation of photothermal performance, PVP-PG can be used as an efficient PTT agent with high photothermal conversion efficiency of ~39.10% and excellent photostability. **(Figure S18-20)** Therefore, based on the above findings, we further evaluated the synergistic effect of RT and PTT in the presence of PVP-PG. More encouragingly, the remaining alive cells of clonogenic survival assay dramatically decreased to 5%, suggesting the combined therapy exhibits a remarkable synergistic effect and enhances the therapeutic efficacy. **(Figure 5d)** This result is further confirmed by the analysis of DNA damage and flow cytometric apoptosis assay. Apparently, the combination of RT with PTT could effectively decrease the radiation dose and reduce the side effects of radiation to achieve the same radiotherapeutic effect. **(Figure 5e)**

3.5 PTT and RT synergetic therapy *in vivo*

In attempt to further investigate the feasibility of using PVP-PG as an effective radiosensitizer, *in vivo* therapeutic experiments were carried out on HeLa tumor

xenograft on BALB/c nude mice. PBS (as control) and PVP-PG were administrated intratumorally, respectively, followed by treatments with X-ray and/or 808 nm laser irradiation. Notably, for the group irradiated with 808 nm laser, the temperature of tumors injected with PVP-PG increases to ~45 °C, a temperature suitable for mild PTT,[30, 63] while the control is not notably heated (~37 °C). **(Figure 6a and Figure S21)** To assess the therapeutic outcome of PVP-PG, the changes of relative tumor volume were recorded every other day for 25 days. **(Figure 6b)** Compared to the control group and the single-treated groups (PVP-PG, X-ray) which showed a rapid progression of tumor volumes, the co-treated (PVP-PG plus X-ray) groups exhibited significant tumor inhibition. This could be further demonstrated by the quantitative antitumor efficacies calculated by the tumor growth inhibition ratio, i.e., PVP-PG (10.21%), X-ray (39.21%) and X-ray plus PVP-PG (81.40%). **(Table S3)** The satisfactory radiosensitizing effect is supposed to be attributed to the manipulation of the TME and enhanced the generation of ROS, leading the death of cancer cells in an apoptosis pathway.[64, 65] Moreover, the combination of RT and PTT produces much enhanced inhibition of cancer tumor growth, indicating the significant *in vivo* synergistic therapeutic effect in radiothermotherapy treatment. This could be attributed to the improvement oxygen level in the TME and thus reduce the hypoxia-associated radioresistance of tumor. As verified by photoacoustic (PA) analysis, compared to the control, the injection of PVP-PG upon NIR irradiation could markedly increase the signal intensity of oxygenated hemoglobin.[66] **(Figure S22)** The similar results shown in the photographs and weights of tumors in all groups

directly exhibited that the growth of HeLa tumor could be effectively inhibited after the administration of PVP-PG followed by X-ray and/or 808 nm laser irradiation. **(Figure 6c-d)** Notably, tumors on mice with injection of PVP-PG were mostly eliminated after both NIR laser and X-ray irradiation, and there was no case of re-growth in our observation period. **(Figure 6e)** Moreover, according to the biodistribution of PVP-PG and BiP_5W_{30} nanoclusters, it was found the PVP-PG could be gradually cleared out from the body during therapeutic period, thereby sharply reducing the potential side effects. **(Figure S23)** Meanwhile, compared to BiP_5W_{30} nanoclusters, the combination of rGO and BiP_5W_{30} nanoclusters can induce higher tumor accumulations and avoid the fast removal from the tumors.

To evaluate the pathological damages to tumors by PVP-PG and further understand the mechanism for the inhibition of tumor growth, the histopathology images of the dissected HeLa tumors are show in **Figure 6f**. The differential destruction of tumor cells could be observed in the H&E images of HeLa tumor tissues for the group co-treated with PVP-PG plus X-ray and the synergistic group after 3-day post-injection. After 25 days, in contrast to partial damage of X-ray alone, almost all of the cells in these two groups are heavily destroyed during therapeutic period, particularly severe cancer necrosis and late-stage apoptosis featuring karyopyknosis and karyorrhexis. Therefore, immunohistochemical analysis was exploited to evaluate DNA damage in tumor section on 3rd day after treatments. **(Figure 6g)** There is a significant DNA double-strand break on tumor sections in both the group co-treated by PVP-PG plus X-ray and the synergistic group, compared to all other groups. These

further demonstrate the potential ability of PVP-PG to the TME-manipulated radiocatalytic enhancement of radiotherapy and radiothermotherapy. Over the therapeutic period of 25 days, there are no obvious difference in body weights of mice in the control and all therapeutic groups, indicating that non-significant toxicity is induced by PVP-PG. **(Figure S24)** Moreover, H&E staining assays of major organs from all of therapeutic groups, as well as blood routine data show no noticeable tissue damage or adverse effect compared to the control, further certifying the high biocompatibility of PVP-PG during the therapeutic process. **(Figure S25-26)** In addition to the treatment efficacy, PVP-PG with high-Z metals and rGO could also act as a dual-modal imaging contrast agent for CT and PA imaging. **(Figures S27-28)** Thus, combination of radiotherapy with different imaging modalities can make it possible to visualize towards sensitizer delivery, internalization, and comprehensive evaluation of therapeutic outcome.[67]

4. Conclusion

In summary, we demonstrated a bismuth heteropolytungstate-based radiocatalytic sensitizer (PVP-PG) for the TME-manipulated enhancement of radiotherapy, based on the unique electron structure and multi-electron properties that is sensitive to X-ray and the TME. Similar to currently reported radiosensitizers, such as gold, PVP-PG is able to amplify X-ray radiation dose at the tumor sites via Compton and Auger effect.[68] Apart from the above contribution, radioactivable PVP-PG can also be stimulated to bring an extra sensitization via "radiocatalytic effect", which ingeniously exploits abundant H_2O_2 and H_2O within the TME to generate more toxic

HO$^\bullet$. The radiotherapeutic outcome can be further improved in virtue of redox-activity of PVP-PG to deplete GSH for disturbance of AOS via "redox-reaction effect". Moreover, NIR-triggered PTT based on PVP-PG can overcome tumor hypoxia microenvironment and synergize with radiotherapy. Taken together, all of the above events hopefully facilitate localized energy deposition in the vicinity of PVP-PG as well as the manipulation of the TME, resulting in better therapeutic outcome and fewer sides effects. To the best of our knowledge, this is the first study that employs both catalytic reaction and redox reaction based on POM for radiotherapy enhancement that is induced by the specific features of TME. Overall, this work not only provides new insight into the design of smart radiosensitizers to achieve more precise and effective radiotherapy, but also extends the application of polyoxometalate used in the biomedical field.

Supporting Information

Supplementary data related to this article can be found at ((will be filled in by the editorial staff))

References

[1] C. Allen, S. Her, D.A. Jaffray, Radiotherapy for cancer: present and future, Adv. Drug Deliv. Rev. 109 (2017) 1-2.
[2] W. Fan, B. Yung, P. Huang, X. Chen, Nanotechnology for multimodal synergistic cancer therapy, Chem. Rev. 117 (2017) 13566-13638.

[3] D. Kwatra, A. Venugopal, S. Anant, Nanoparticles in radiation therapy: a summary of various approaches to enhance radiosensitization in cancer, Transl. Cancer Res. 2 (2013) 330-342.

[4] C. Hegedus, K. Kovacs, Z. Polgar, Z. Regdon, E. Szabo, A. Robaszkiewicz, H.J. Forman, A. Martner, L. Virag, Redox control of cancer cell destruction, Redox Biol. 16 (2018) 59-74.

[5] G. Song, L. Cheng, Y. Chao, K. Yang, Z. Liu, Emerging nanotechnology and advanced materials for cancer radiation therapy, Adv. Mater. 29 (2017) 1700996.

[6] W. Fan, W. Bu, Z. Zhang, B. Shen, H. Zhang, Q. He, D. Ni, Z. Cui, K. Zhao, J. Bu, J. Du, J. Liu, J. Shi, X-ray radiation-controlled NO-release for on-demand depth-independent hypoxic radiosensitization, Angew. Chem. Int. Ed. 54 (2015) 14026-14030.

[7] P. Vaupel, Tumor microenvironmental physiology and its implications for radiation oncology, Semin. Radiat. Oncol. 14 (2004) 198-206.

[8] V.V. Khramtsov, R.J. Gillies, Janus-faced tumor microenvironment and redox, Antiox. Red. Sign. 21 (2014) 723-729.

[9] J. Bai, X. Jia, W. Zhen, W. Cheng, X. Jiang, A facile ion-doping strategy to regulate tumor microenvironments for enhanced multimodal tumor theranostics, J. Am. Chem. Soc. 140 (2018) 106-109.

[10] T.P. Szatrowski, C.F. Nathan, Production of large amounts of hydrogen-peroxide by human tumor-cells, Cancer Res. 51 (1991) 794-798.

[11] J.M. Brown, W.R. Wilson, Exploiting tumour hypoxia in cancer treatment, Nat. Rev. Cancer 4 (2004) 437-447.

[12] H. Harada, Hypoxia-inducible factor 1-mediated characteristic features of cancer cells for tumor radioresistance, J. Radiat. Res. 57 (2016) i99-i105.

[13] S.S. Sabharwal, P.T. Schumacker, Mitochondrial ROS in cancer: initiators, amplifiers or an Achilles' heel?, Nat. Rev. Cancer 14 (2014) 709-721.

[14] M.H. Lee, Z. Yang, C.W. Lim, Y.H. Lee, S. Dongbang, C. Kang, J.S. Kim, Disulfide-cleavage-triggered chemosensors and their biological applications, Chem. Rev. 113 (2013) 5071-5109.

[15] H. Lin, Y. Chen, J. Shi, Nanoparticle-triggered in situ catalytic chemical reactions for tumour-specific therapy, Chem. Soc. Rev. 47(2018) 1938-1958.

[16] J. Wang, J. Yi, Cancer cell killing via ROS: To increase or decrease, that is the question, Cancer Biol. Ther. 7 (2014) 1875-1884.

[17] José M. Estrela, A. Ortega, S. Mena, J.A. Sirerol, E. Obrador, Glutathione in metastases: from mechanisms to clinical applications, Crit. Rev. Clin. Lab. Sci. 53 (2015) 253-267.

[18] C. Zhang, W. Bu, D. Ni, S. Zhang, Q. Li, Z. Yao, J. Zhang, H. Yao, Z. Wang, J. Shi, Synthesis of iron nanometallic glasses and their application in cancer therapy by a localized Fenton reaction, Angew. Chem. Int. Ed. 55 (2016) 2101-2106.

[19] Z. Yang, Y. Dai, C. Yin, Q. Fan, W. Zhang, J. Song, G. Yu, W. Tang, W. Fan, B.C. Yung, J. Li, X. Li, X. Li, Y. Tang, W. Huang, J. Song, X. Chen, Activatable semiconducting theranostics: simultaneous generation and ratiometric photoacoustic imaging of reactive oxygen species in vivo, Adv. Mater. 30 (2018) 1707509.

[20] Z. Jin, Y. Wen, L. Xiong, T. Yang, P. Zhao, L. Tan, T. Wang, Z. Qian, B.L. Su, Q. He, Intratumoral H_2O_2-triggered release of CO from a metal carbonyl-based nanomedicine for efficient CO therapy, Chem. Commun. 53 (2017) 5557-5560.

[21] T. Yamamori, H. Yasui, M. Yamazumi, Y. Wada, Y. Nakamura, H. Nakamura, O. Inanami, Ionizing radiation induces mitochondrial reactive oxygen species production accompanied by upregulation of mitochondrial electron transport chain function and mitochondrial content under control of the cell cycle checkpoint, Free Radic. Biol. Med. 53 (2012) 260-270.

[22] E.I. Azzam, J.P. Jay-Gerin, D. Pain, Ionizing radiation-induced metabolic oxidative stress and prolonged cell injury, Cancer Lett. 327 (2012) 48-60.

[23] A.K. Hauser, M.I. Mitov, E.F. Daley, R.C. McGarry, K.W. Anderson, J.Z. Hilt, Targeted iron oxide nanoparticles for the enhancement of radiation therapy, Biomaterials 105 (2016) 127-135.

[24] Y. Yong, L.J. Zhou, S.S. Zhang, L. Yan, Z.J. Gu, G.J. Zhang, Y.L. Zhao, Gadolinium polytungstate nanoclusters: a new theranostic with ultrasmall size and versatile properties for dual-modal MR/CT imaging and photothermal therapy/radiotherapy of cancer, NPG Asia Mater. 8 (2016) e273.

[25] A. Detappe, E. Thomas, M.W. Tibbitt, S. Kunjachan, O. Zavidij, N. Parnandi, E. Reznichenko, F. Lux, O. Tillement, R. Berbeco, Ultrasmall silica-based bismuth gadolinium nanoparticles for dual magnetic resonance-computed tomography image guided radiation therapy, Nano Lett. 17 (2017) 1733-1740.

[26] Y. Yong, C. Zhang, Z. Gu, J. Du, Z. Guo, X. Dong, J. Xie, G. Zhang, X. Liu, Y. Zhao, Polyoxometalate-based radiosensitization platform for treating hypoxic tumors by attenuating radioresistance and enhancing radiation response, ACS Nano 11 (2017) 7164-7176.

[27] A. Bijelic, M. Aureliano, A. Rompel, Polyoxometalates as potential next-generation metallodrugs in the combat against cancer, Angew. Chem. Int. Ed. (2018), DOI: 10.1002/anie.201803868.

[28] Q. Zhai, L. Zhang, X. Zhao, H. Chen, D. Yin, J. Li, A novel iron-containing polyoxometalate heterogeneous photocatalyst for efficient 4-chlorophennol degradation by H_2O_2 at neutral pH, Appl. Surf. Sci. 377 (2016) 17-22.

[29] Q. Xiang, J. Yu, M. Jaroniec, Graphene-based semiconductor photocatalysts, Chem. Soc. Rev. 41 (2012) 782-796.

[30] T. Paunesku, S. Gutiontov, K. Brown, G.E. Woloschak, Radiosensitization and nanoparticles, Cancer Treat. Res. 166 (2015) 151-171.

[31] I. Creaser, M.C. Heckel, R.J. Neitz, M.T. Pope, Rigid nonlabile polyoxometalate cryptates $[ZP_5W_{30}O_{110}]^{(15-n)-}$ that exhibit unprecedented selectivity for certain lanthanide and other multivalent cations, Inorg. Chem. 32 (1993) 1573-1578.

[32] W. S. Hummers Jr., R. E. Offeman, Preparation of graphitic oxide, J. Am. Chem. Soc. 80 (1958) 1339-1339.

[33] L. Yan, Y.N. Chang, W. Yin, X. Liu, D. Xiao, G. Xing, L. Zhao, Z. Gu, Y. Zhao, Biocompatible and flexible graphene oxide/upconversion nanoparticle hybrid film for optical pH sensing, Phys. Chem. Chem. Phys. 16 (2014) 1576-1582.

[34] R.J. Liu, G.J. Zhang, H.B. Cao, S.J. Zhang, Y.B. Xie, A. Haider, U. Kortz, B.H. Chen, N.S. Dalal, Y.S. Zhao, L.J. Zhi, C.X. Wu, L.K. Yan, Z.M. Su, B. Keita, Enhanced proton and electron reservoir abilities of polyoxometalate grafted on graphene for high-performance hydrogen evolution, Energy Environ. Sci. 9 (2016) 1012-1023.

[35] W. Yin, J. Yu, F. Lv, L. Yan, L.R. Zheng, Z. Gu, Y. Zhao, Functionalized nano-MoS_2 with peroxidase catalytic and near-infrared photothermal activities for safe and synergetic wound antibacterial applications, ACS Nano 10 (2016) 11000-11011.

[36] P.a. Ma, H. Xiao, C. Yu, J. Liu, Z. Cheng, H. Song, X. Zhang, C. Li, J. Wang, Z. Gu, J. Lin, Enhanced cisplatin chemotherapy by iron oxide nanocarrier-mediated generation of highly toxic reactive oxygen species, Nano Lett. 17 (2017) 928-937.

[37] E. Ju, K. Dong, Z. Chen, Z. Liu, C. Liu, Y. Huang, Z. Wang, F. Pu, J. Ren, X. Qu, Copper(II)-graphitic carbon nitride triggered synergy: Improved ROS generation and reduced glutathione levels for enhanced photodynamic therapy, Angew. Chem. Int. Ed. 128 (2016) 11639-11643.

[38] A. Iwase, Y.H. Ng, Y. Ishiguro, A. Kudo, R. Amal, Reduced graphene oxide as a solid-state electron mediator in Z-scheme photocatalytic water splitting under visible light, J. Am. Chem. Soc. 133 (2011) 11054-11057.

[39] J. Du, Z. Gu, L. Yan, Y. Yong, X. Yi, X. Zhang, J. Liu, R. Wu, C. Ge, C. Chen, Y. Zhao, Poly(Vinylpyrollidone)- and selenocysteine-modified Bi_2Se_3 nanoparticles enhance radiotherapy efficacy in tumors and promote radioprotection in normal tissues, Adv. Mater. 29 (2017) 1701268.

[40] A. Miiller, M.T. Pope, Polyoxometalate Chemistry: An old field with new dimensions in several disciplines, Angew. Chem. Int. Ed. 30 (1991) 34-48.

[41] S.S. Wang, G.Y. Yang, Recent advances in polyoxometalate-catalyzed reactions, Chem. Rev. 115 (2015) 4893-4962.

[42] A. Hiskia, A. Mylonas, E. Papaconstantinou, Comparison of the photoredox properties of polyoxometallates and semiconducting particles, Chem. Soc. Rev. 30 (2001) 62-69.

[43] C. Zhang, W. Bu, D. Ni, C. Zuo, C. Cheng, Q. Li, L. Zhang, Z. Wang, J. Shi, A polyoxometalate cluster paradigm with self-adaptive electronic structure for acidity/reducibility-specific photothermal conversion, J. Am. Chem. Soc. 138 (2016) 8156-8164.

[44] E. Papaconstantinou, A. Hiskia, A. Troupis, Photocatalytic processes with tungsten oxygen anion clusters, Front. Biosci. 8 (2003) s813-825.

[45] M. Babaei, M. Ganjalikhani, The potential effectiveness of nanoparticles as radio sensitizers for radiotherapy, Bioimpacts 4 (2014) 15-20.

[46] C. Zhang, K. Zhao, W. Bu, D. Ni, Y. Liu, J. Feng, J. Shi, Marriage of scintillator and semiconductor for synchronous radiotherapy and deep photodynamic therapy with diminished oxygen dependence, Angew. Chem. Int. Ed. 54 (2015) 1770-1774.

[47] S.H. Yun, S.J.J. Kwok, Light in diagnosis, therapy and surgery, Nat. Biomed. Eng. 1 (2017) 0008.

[48] S.P. Sahu, E.L. Cates, X-ray radiocatalytic activity and mechanisms of bismuth complex oxides, J. Phys. Chem. C 121 (2017) 10538-10545.

[49] Z. Guo, S. Zhu, Y. Yong, X. Zhang, X. Dong, J. Du, J. Xie, Q. Wang, Z. Gu, Y. Zhao, Synthesis of BSA-Coated $BiOI@Bi_2S_3$ semiconductor heterojunction nanoparticles and their applications for radio/photodynamic/photothermal synergistic therapy of tumor, Adv. Mater. 29 (2017) 1704136.

[50] K. Vinodgopal, D.E. Wynkoop, P.V. Kamat, Environmental photochemistry on semiconductor surfaces: Photosensitized degradation of a textile azo dye, acid orange 7, on TiO_2 particles using visible light, Environ. Sci. Technol. 30 (1996) 1660-1666.

[51] F. Gao, X.Y. Chen, K.B. Yin, S. Dong, Z.F. Ren, F. Yuan, T. Yu, Z. Zou, J.M. Liu, Visible-light photocatalytic properties of weak magnetic $BiFeO_3$ nanoparticles, Adv. Mater. 19 (2007) 2889-2892.

[52] L. Yan, Z. Gu, X. Zheng, C. Zhang, X. Li, L. Zhao, Y. Zhao, Elemental bismuth–graphene heterostructures for photocatalysis from ultraviolet to infrared light, ACS Catal. 7 (2017) 7043-7050.

[53] G. Jin, S.M. Wang, W.L. Chen, C. Qin, Z.M. Su, E.B. Wang, A photovoltaic system composed of a keplerate-type polyoxometalate and a water-soluble poly(p-phenylenevinylene) derivative, J. Mater. Chem. A 1 (2013) 6727-6730.

[54] D. Schmaljohann, Thermo- and pH-responsive polymers in drug delivery, Adv. Drug Deliv. Rev. 58 (2006) 1655-1670.

[55] H.C. Huang, C.J. Lin, W.J. Liu, R.R. Jiang, Z.F. Jiang, Dual effects of curcumin on neuronal oxidative stress in the presence of Cu(II), Food Chem. Toxicol. 49 (2011) 1578-1583.

[56] J.M. Estrela, A. Ortega, E. Obrador, Glutathione in cancer biology and therapy, Crit. Rev. Clin. Lab. Sci. 43 (2006) 143-181.

[57] L.S. Lin, J. Song, L. Song, K. Ke, Y. Liu, Z. Zhou, Z. Shen, J. Li, Z. Yang, W. Tang, G. Niu, H.H. Yang, X. Chen, Simultaneous Fenton-like ion delivery and glutathione depletion by MnO_2-based nanoagent to enhance chemodynamic therapy, Angew. Chem. Int. Ed. 57 (2018) 4902-4906.

[58] Y. Liu, W. Zhen, L. Jin, S. Zhang, G. Sun, T. Zhang, X. Xu, S. Song, Y. Wang, J. Liu, H. Zhang, All-in-One theranostic nanoagent with enhanced reactive oxygen species generation and modulating tumor microenvironment ability for effective tumor eradication, ACS Nano 12 (2018) 4886-4893.

[59] H. Fan, G. Yan, Z. Zhao, X. Hu, W. Zhang, H. Liu, X. Fu, T. Fu, X.B. Zhang, W. Tan, A smart photosensitizer-manganese dioxide nanosystem for enhanced photodynamic therapy by reducing glutathione levels in cancer cells, Angew. Chem. Int. Ed. 55 (2016) 5477-5482.

[60] N.A. Franken, H.M. Rodermond, J. Stap, J. Haveman, C. van Bree, Clonogenic assay of cells in vitro, Nat. Protoc. 1 (2006) 2315-2319.

[61] W.M. Bonner, C.E. Redon, J.S. Dickey, A.J. Nakamura, O.A. Sedelnikova, S. Solier, Y. Pommier, γ-H2AX and cancer, Nat. Rev. Cancer 8 (2008) 957-967.

[62] Q. He, D.O. Kiesewetter, Y. Qu, X. Fu, J. Fan, P. Huang, Y. Liu, G. Zhu, Y. Liu, Z. Qian, X. Chen, NIR-responsive on-demand release of CO from metal carbonyl-caged graphene oxide nanomedicine, Adv. Mater. 27 (2015) 6741-6746.

[63] A. Li, X. Li, X. Yu, W. Li, R. Zhao, X. An, D. Cui, X. Chen, W. Li, Synergistic thermoradiotherapy based on PEGylated Cu_3BiS_3 ternary semiconductor nanorods with strong absorption in the second near-infrared window, Biomaterials 112 (2017) 164-175.

[64] J. Noh, B. Kwon, E. Han, M. Park, W. Yang, W. Cho, W. Yoo, G. Khang, D. Lee, Amplification of oxidative stress by a dual stimuli-responsive hybrid drug enhances cancer cell death, Nat. Commun. 6 (2015) 6907.

[65] M. Huo, L. Wang, Y. Chen, J. Shi, Tumor-selective catalytic nanomedicine by nanocatalyst delivery, Nat. Commun. 8 (2017) 357.

[66] X. Cheng, Y. Yong, Y. Dai, X. Song, G. Yang, Y. Pan, C. Ge, Enhanced radiotherapy using bismuth sulfide nanoagents combined with photo-thermal treatment, Theranostics 7 (2017) 4087-4098.

[67] H. Jadvar, X. Chen, W. Cai, U. Mahmood, Radiotheranostics in cancer diagnosis and management, Radiology 286 (2018) 388-400.

[68] S. Her, D.A. Jaffray, C. Allen, Gold nanoparticles for applications in cancer radiotherapy: Mechanisms and recent advancements, Adv. Drug Deliv. Rev. 109 (2017) 84-101.
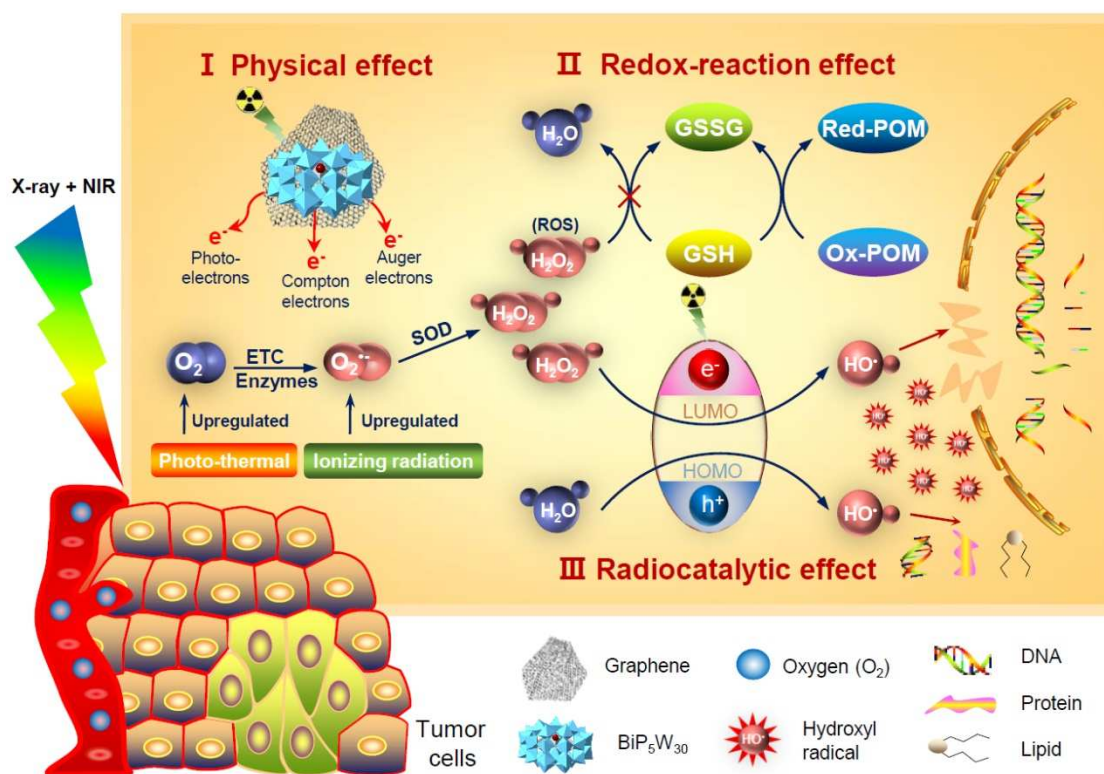
Figure 1. Principle of the TME-manipulated radiocatalytic sensitizer. Schematic representation of mechanism of PVP-PG on the amplification of X-ray radiation dose deposition and the manipulation of TME for reversing tumor radioresistance through depleting GSH concentration, converting H_2O_2 to $HO^{\bullet}$ as well as improving oxygen level in tumors.
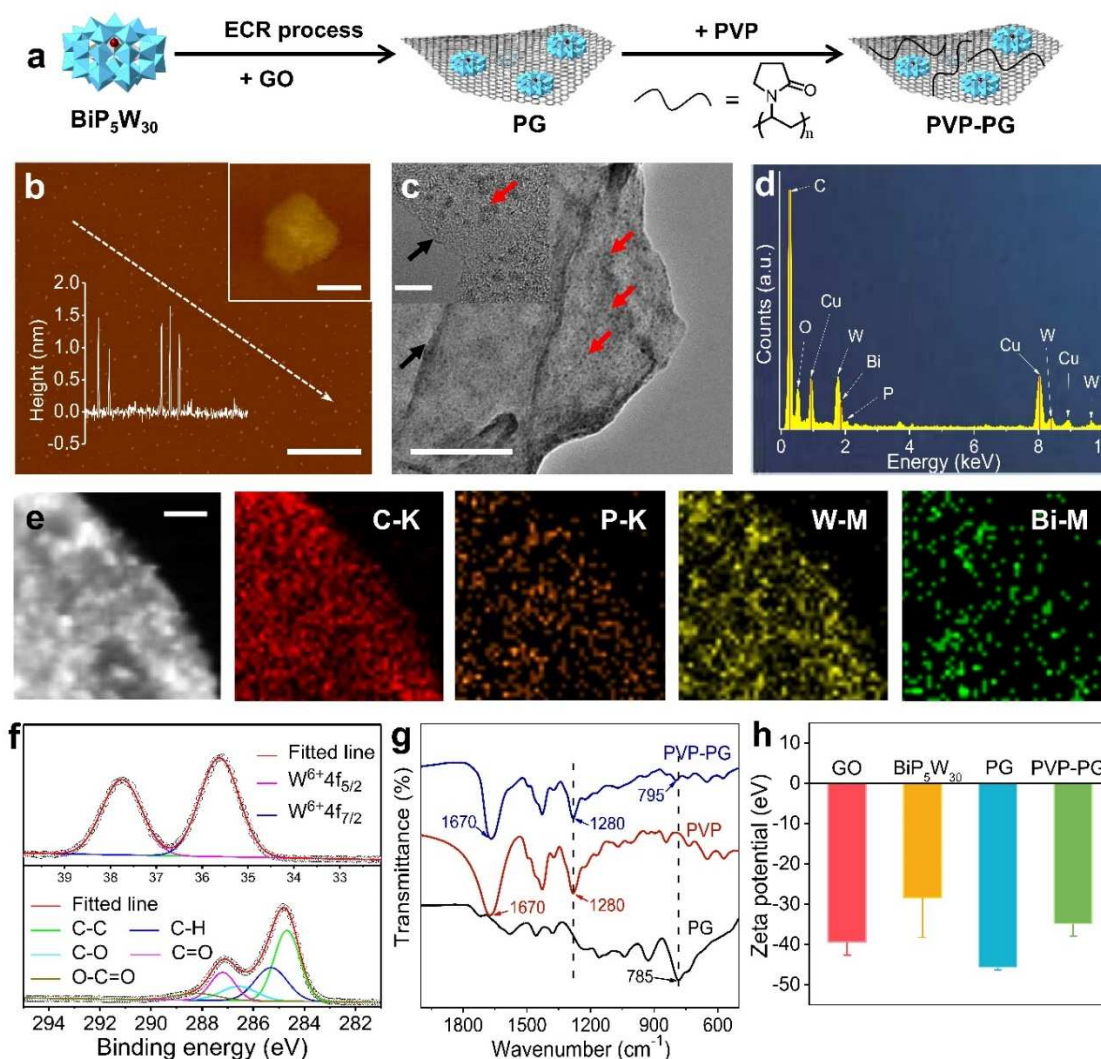
Figure 2. Synthesis and characterization of PVP-PG. (**a**) Schematic diagram of preparation of PVP-PG. (**b**) AFM image of PG. (Scale bar: 1 μm; insert: 20 nm). (**c**) A TEM image of PVP-PG. Inset: an enlarged TEM image. Red arrows indicate BiP_5W_{30} clusters and black arrow indicates rGO. (Scale bar: 10 nm; insert: 5 nm). (**d**) EDS analysis of PVP-PG. (**e**) The magnified TEM image and corresponding EDS element mapping images. (Scale bars: 5 nm). (**f**) Deconvolution of high-resolution W4f (up) and C1s (down) XPS spectra. (**g**) FT-IR spectra of PG, PVP, and PVP-PG, respectively. (**h**) Zeta potential of aqueous dispersion of GO, BiP_5W_{30}, PG and PVP-PG.
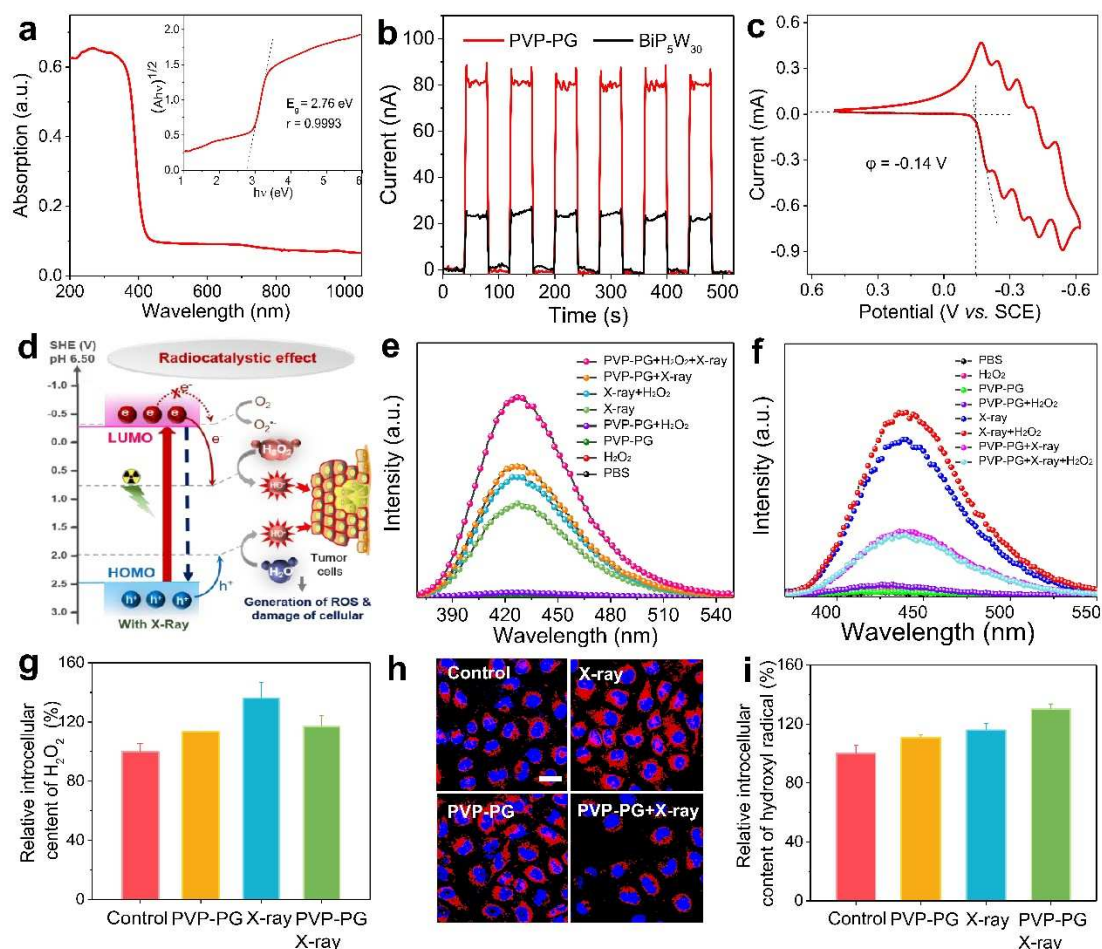
Figure 3. Radiocatalysis effect of PVP-PG. (**a**) Diffuse reflectance spectrum of PVP-PG. Inset: Plot transformed according to the Kubelka-Munk function versus energy of light. The dashed line is the tangent of the curve. (**b**) X-ray induced photocurrent with BiP_5W_{30} clusters and PVP-PG, respectively, responded to the on/off of X-ray irradiation. (**c**) The cyclic voltammogram of PVP-PG in 0.5 M H_2SO_4. Scan rate: 10 mV/s. (**d**) Schematic illustration of mechanism of PVP-PG. (**e**) Fluorescence spectra of TAOH after various treatments. (**f**) Fluorescence spectra of TAOH after various treatments in the presence of $S_2O_8^{2-}$. (**g**) Relative content of H_2O_2 in HeLa cells after different treatments. (**h**) Confocal fluorescence images of H_2O_2 in HeLa cells after different treatments. (scale bar: 50 μm). (**i**) Relative content of $HO^•$ in HeLa cells after different treatments.
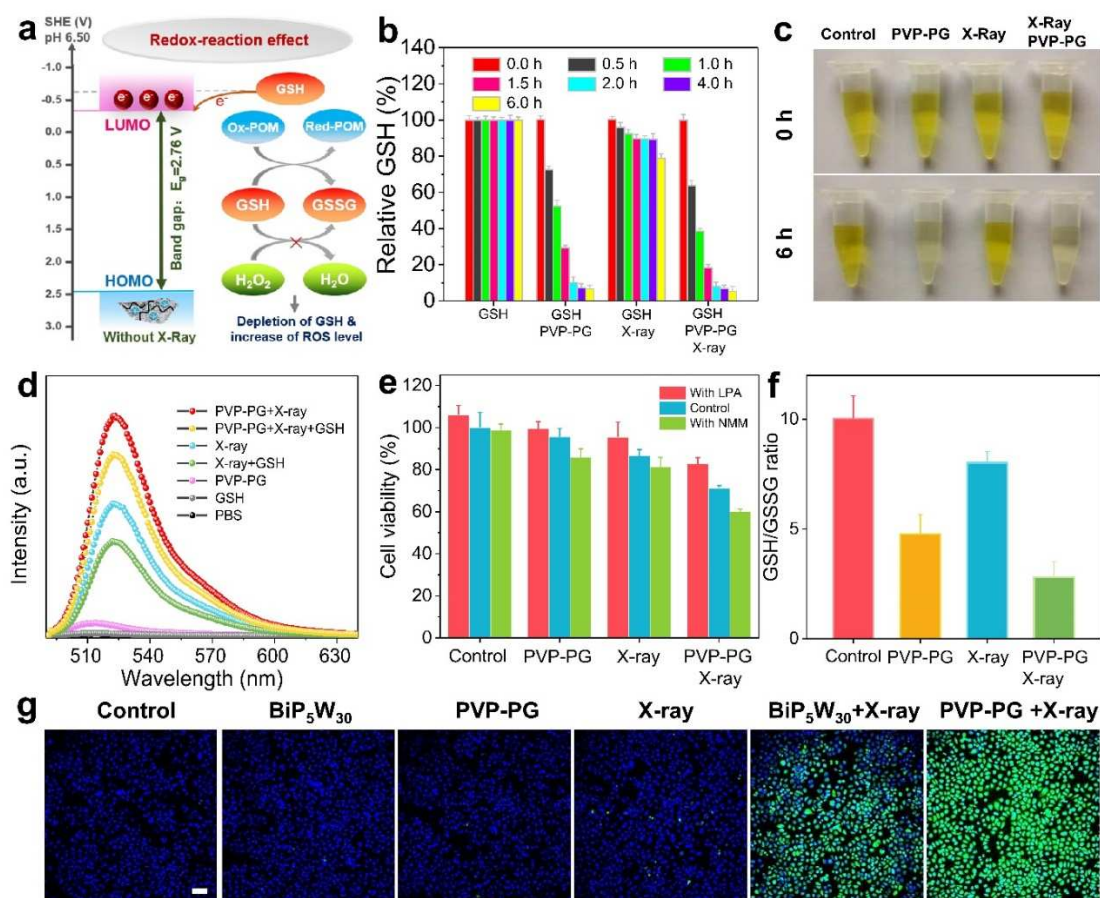
Figure 4. Redox effect of PVP-PG. (**a**) Schematic illustration of mechanism of PVP-PG. (**b**) Relative GSH amount after different treatments. (**c**) Photographs of color change of GSH after various treatments at 0 h and 6 h intervals under 37 °C. (**d**) Fluorescence spectra of DCF mixed with PVP-PG after various treatments with or without GSH. (**e**) *In vitro* cytotoxicity of PVP-PG with or without LPA and NMM after 24 h of different treatments. (**f**) Intracellular GSH/GSSG ratios in HeLa cells after different treatments. (**g**) Fluorescence spectra of DCF on cells after different treatments. (scale bar: 100 μm).
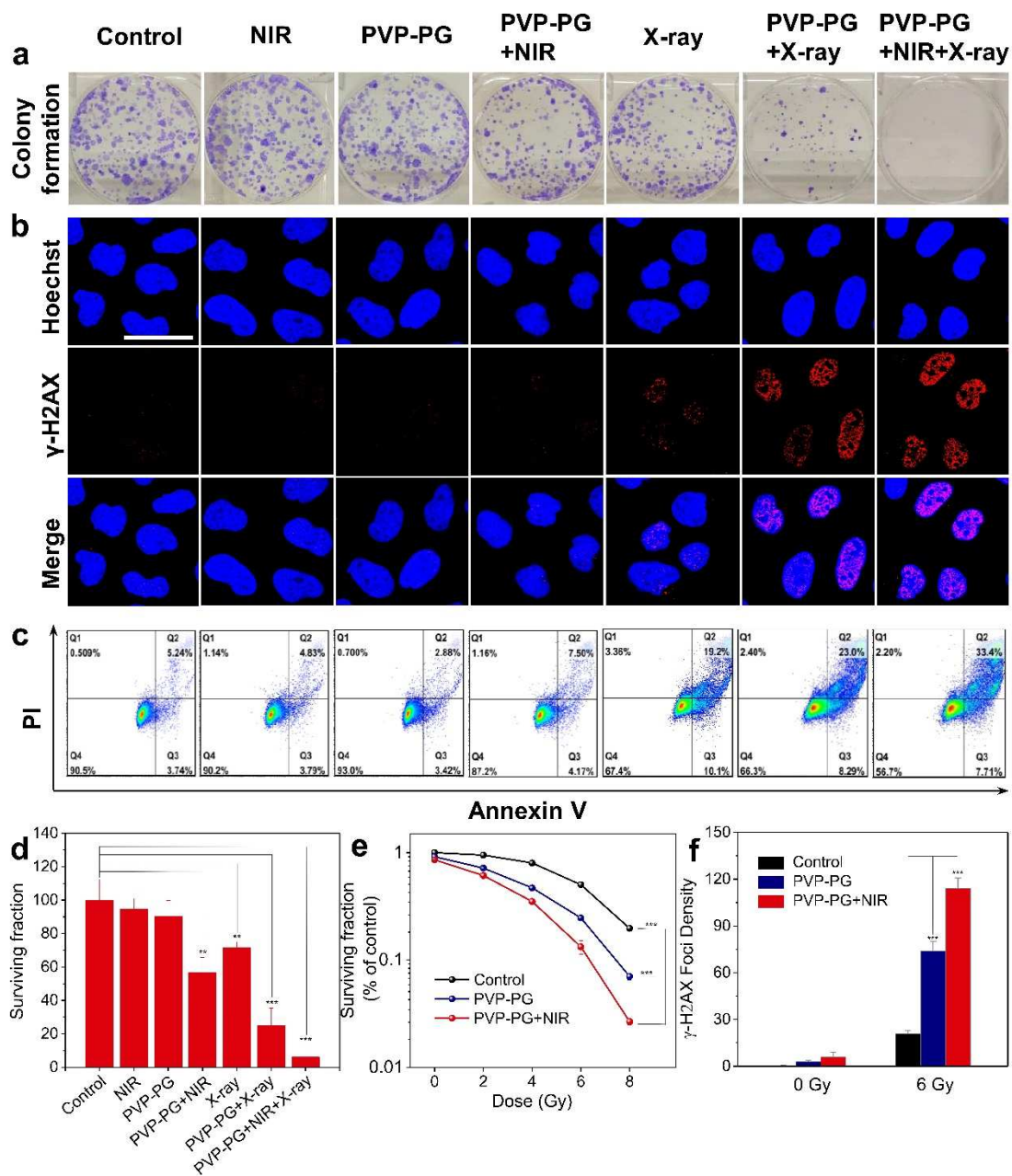
Figure 5. PTT and RT synergetic therapy *in vitro*. (**a**) Clonogenic assay after different treatments with clones produced by HeLa cells. (**b**) Qualitative representation of γ-H2AX foci formation with or without X-ray irradiation, 30 min post-irradiation (scale bar: 50 μm). (**c**) Qualitative flow cytometry data plot indicating the increase in apoptosis of HeLa cells after different treatments for 24 h. (**d**) Responding survival fraction of HeLa cells with different treatments after 10-day colony. (**e**) Clonogenic survival assay of HeLa cells treated with or without PVP-PG under series of radiation doses at 0, 2, 4, 6, and 8 Gy. (**f**) Quantitative analysis of number of γ-H2AX foci per cell. The error bars represent the standard error of mean of at least three replicates. P values: $^{*}P < 0.05$, $^{**}P < 0.01$, $^{***}P < 0.001$.
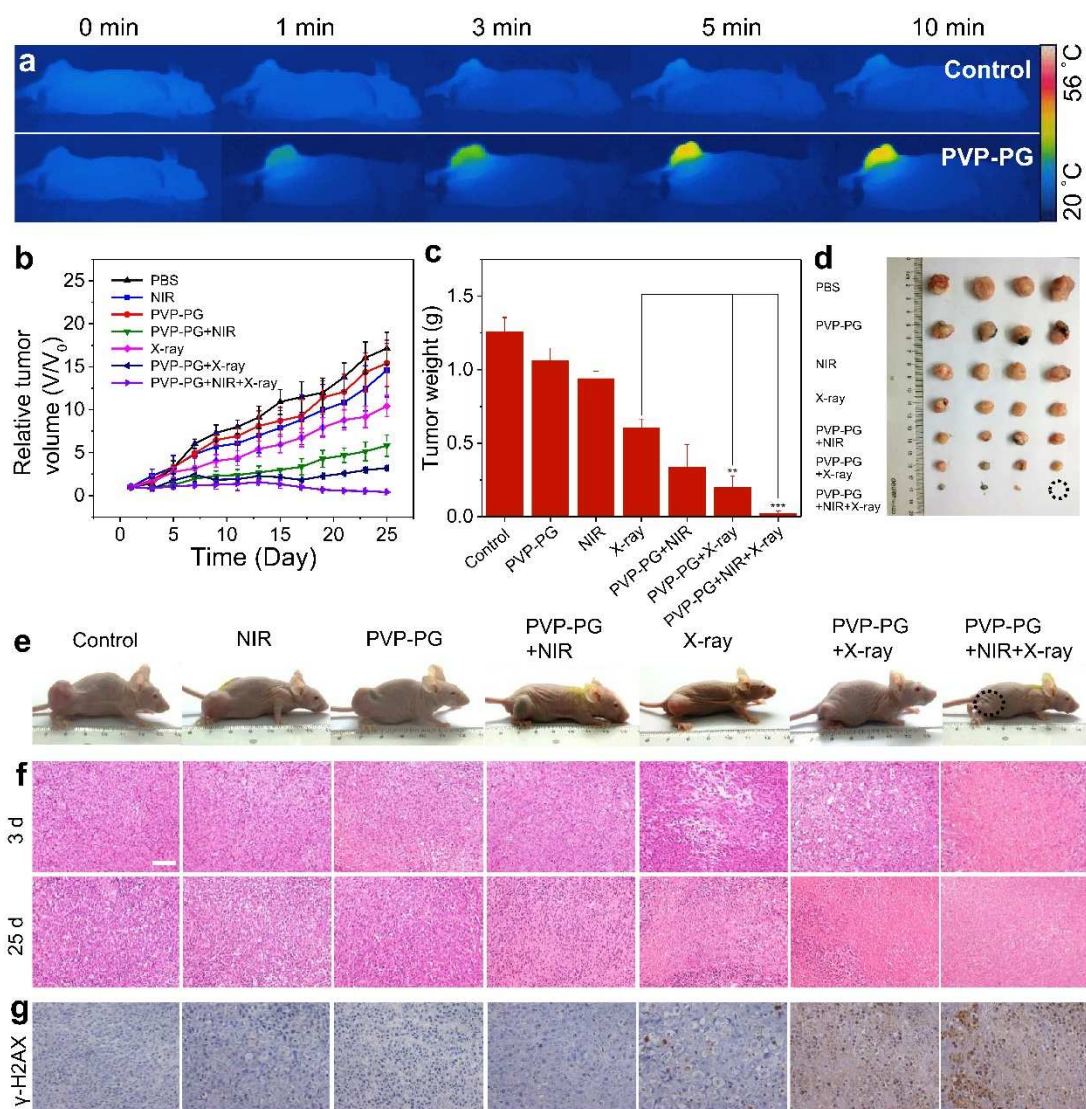
Figure 6: PTT and RT synergetic therapy *in vivo*. (**a**) Representative thermal response in HeLa tumor-bearing mice with intratumoral injection of PBS and PVP-PG. (**b**) Relative tumor volumes in HeLa tumor-bearing mice after different treatments. (n=4) (**c**) The tumor weights of dissected tumors from each group after 25 days of therapy. (**d**) Digital photographs of the dissected tumors each group. Black circle indicates the eliminated tumors. (**e**) Digital photographs of representative mice from each group captured on 25th day for showing the effects of different therapeutic outcomes. (**f**) H&E of tumor sections from each group on 3rd (up) and 25th (down) day under different treatments. (scale bar: 50 μm). (**g**) γ-H2AX staining representing the DNA double-strand breaks in the tumor sections on 3rd day. Damaged cells are brown and viable cells are blue. (scale bar: 50 μm), ***$P < 0.001$.

Table of contents
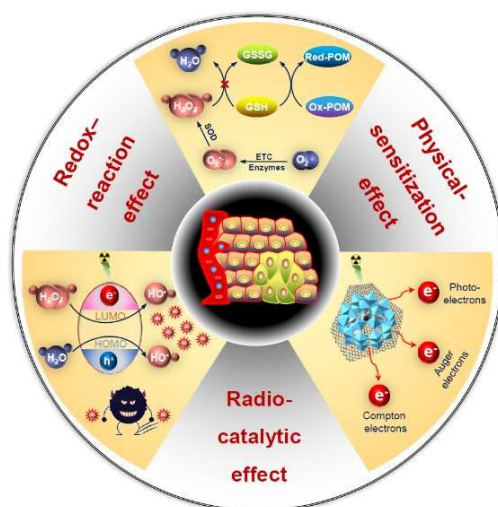
The tumor microenvironment-manipulated bismuth heteropolytungstate nanoclusters could serve as a simple yet powerful radiocatalytic sensitizer for achieving tumor-specific radiotherapy by simultaneously increasing X-ray dose deposition and reversing the radio-resistance through the improvement of hypoxia environment, depletion of glutathione, and radiocatalytic conversion of overproduced hydrogen peroxide into highly toxic hydroxyl radical.